Peer-reviewed version available at *Sensors* **2020**, *20*, 4762; doi:10.3390/s20174762

Article

Marine Boundary Layer Height obtained by New Numerical Regularization Method Based on GPS Radio Occultation Data

Jianyin Zhou [1], Jie Xiang [1,*] and Sixun Huang [1,2]

[1] College of Meteorology and Oceanography, National University of Defense Technology, Nanjing, China
[2] State Key Laboratory of Satellite Ocean Environment Dynamics, Second Institute of Oceanography, State Oceanic Administration, Hangzhou, China
* Correspondence: xiangjie2021@163.com

Abstract: The boundary layer height (BLH) distinguishes the interface between the lower and free atmosphere, which is a key variable in numerical simulation, aerosol, and environmental pollution studies. Thus, the goal of this work is to propose a novel method conjuncting with numerical regularization to analysis climate characteristics of the marine boundary layer height (MBLH) using 2007-2011 GPS-RO data from the COSMIC mission. While traditionally, the difference method has been used to achieve this aim, herein, we propose an innovative method, in which the bending angle profile gradient was calculated using the numerical regulation method where the regulation parameters are determined by the double-parameter model function method. Then, the MBLH was determined by employing the maximum gradient method to ascertain the height corresponding to the smallest gradient. The results show a correlation between currents and the MBLH—a relationship that has not been previously demonstrated. A low MBLH is associated with seasons and regions where cold ocean currents are prevailing; whereas a high MBLH is observed in the seasons and places where warm currents are prevailing. This correlation was validated by comparing the obtained results with different occultation data—i.e., atmprf and echprf—which also established that atmprf is more sensitive to convective cloud top capture. In seas with active convection, the armprf calculated bending angle is higher than that from echprf. Subsequently, the standard deviation was used to express the MBLH confidence level. The results show that the MBLH standard deviation is highest in low latitudes and lowest in the middle and high latitudes. Furthermore, we analyzed the interannual MBLH variation trend, which displayed a seasonal variation and spatial distribution corresponding with the current and subsolar point. Finally, we conducted a case study in the South China Sea, and identified a distinctive seasonal change and downward trend.

Keywords: Marine boundary layer height; Numerical regulation method; Double-parameter model function method; COSMIC data; Climate characteristics.

1. Introduction

Atmospheric physical processes in the marine boundary layer mostly occur at the sub-grid scale [1,2], where sensible heat flux, water vapor flux, turbulent vertical transport, sea breeze intensity, and sea waves impact the marine boundary layer height (MBLH) [3]. Thus, accurately analyzing the MBLH climate characteristics is particularly important, as MBLH is a key variable for the boundary layer parameterization scheme in the climate numerical model.

In present studies, the data used to detect the boundary layer height mainly include radiosonde data by[4-6], various types of radar data[7-11], ERA-Interim reanalysis data by (Engeln and Teixeira, 2013), and GPS occultation data by (Chan and Wood, 2013; Guo et al., 2011), etc.

Peer-reviewed version available at Sensors 2020, 20, 4762; doi:10.3390/s20174762

Radar and radiosonde data are inappropirate for climate change analysis at the MBLH due to their limited spatial distribution;while ERA-Interim data is model-based reanalysis data, which not only has coarse resolution but also inherent model errors. However, the Formosa Satellite Mission 3 (FORMOSAT-3)/Constellation Observing System for Meteorology, Ionosphere, and Climate (COSMIC) satellites data has a resolution of: ~ 100m at 0 m-1 km, ~ 200m at 1 - 2 km, and ~ 300 – 400 m at 2 -5 km. Further advantages include high vertical resolution, all-weather, global exploration, which compensates for the lack of observatory data in the ocean area. Based on the properties described above, cosmic occultation data can be reliably used to characterize the global MBLH climate change.

Given that the boundary layer height (i.e., the top of the boundary layer) plays a role in improving weather forecast accuracy, climate prediction, and air quality research[5,11-13], numerous studies have recently been conducted on boundary layer height changes. Basha and Ratnam [14] used the maximum gradient method in conjunction with 2.5 year sounding data from a tropical station at Gadanki to determine the boundary layer height , and study its seasonal and daily changes at the station; Ao, et al. [15] used the COSMIC/FORMOSAT-3 occultation data from 2006-2009 and the ECMWF's data (ERA-Int) to determine the boundary layer height by assessing the minimum refractivity height and water vapor pressure gradient, then using its significance coefficient, as proposed in 2008, as the basis for test results credibility; Yehui, et al. [16] used the bulk Richardson number method to determine the boundary layer height, then roughy esimated the boundary layer height change trend throughout the European region; Chan and Wood [17] improved on the maximum gradient method proposed by Sokolovskiy, et al. [18], and analyzed the seasonal cycle characteristics of the global boundary layer height; Shu-peng, et al. [19] analyzed the seasonal and daily changes in the MBLH of the Southeast Pacific Ocean; Guo, Li, Cohen, Li, Chen, Xu, Liu, Yin, Hu and Zhai [5] used the bulk Richardson Number method in conjunction with 1976 - 2016 radiosonde data from CRN to determine the boundary layer height, then studied the boundary layer height spatiotemporal variation trend over China; Chien, et al. [20] studied the MBLH over the western North Pacific (WNP) based on COSMIC profiles in addition to three other sources of data. In this novel work, we proposed a new method—a numerical differential model function method, for determining the boundary layer height, then applied it to examine the MBLH global seasonal variation characteristics and inter-annual changes near the South China Sea.

Unlike the BLH on land, which exhibits significant diurnal fluctuations, the MBLH changes relatively slowly over space and time since the ocean serves as its underlying surface. Essentially, the strong seawater mixing makes the surface physical properties uniform. In addition, due to the massive heat capacity, even if a large amount of heat from the sun is absorbed, the temperature of the underlying surface, which forces the boundary layer to rise, will not significantly change [3]. Drastic changes in MBLH mostly occur in small and medium scale weather systems; in response to different air masses on the sea surface undergoing vertical movement and convection under forcing. Such processes cause increased turbulent mixing in the mixed layer, thereby raising the MBLH [21].

In this work, we used the numerical differential regularization method, combined with COSMIC occultation bending angle data, to analyze the MBLH climate change trend in the global ocean. We begin by introducing the data and methods used in our research; then demonstrate MBLH's global distribution, seasonal variation, and inter-annual variation characteristics; and finally summarize our findings.

Peer-reviewed version available at Sensors 2020, 20, 4762; doi:10.3390/s20174762

2. Data

GPS radio occultation observation technology utilizes the radio waves' additional phase delay and amplitude change in the atmosphere, which is caused by the interaction of electromagnetic waves emitted from high and low orbit satellites. Furthermore, it can also obtain the radio waves' bending angle profile due to the atmospheric refraction gradient. Assuming local spherical symmetry of the Earth's atmosphere, the nonlocal refractive index can be obtained, via Abel transformation (2), because the bending angle and refractivity have a one to one mapping relationship (1). In the process of obtaining the bending angle and refractivity, we found that the former has more advantages than the latter when calculating the ABL height. First, the bending angle data is directly obtained from the original observed optical path length, which has relatively limited observational error characteristics and is more sensitive to the vertical distribution of meteorological elements in the atmosphere. Second, it offers an alternative to calculating the refractivity profile using the Abelian inverse integral. Thus, it avoids diffusion of the bending angle observation error on the refractivity, which is a side effect of a poorly posed Abelian integral, and circumvents the unnecessary error caused by the Abelian weak singular kernel in the process of numerical discrete calculation.

$$\alpha(a) = -2a\int_{r_0}^{\infty} \frac{\frac{d\ln n}{dr}}{\sqrt{n^2r^2 - a^2}}dr \tag{1}$$

$$n^{\mathrm{GPS}}(r) = \exp\left(\frac{1}{\pi}\int_{r}^{\infty} \frac{\alpha(x)}{\sqrt{x^2 - a^2}}\mathrm{d}x\right) \tag{2}$$

In this study, we employed Global Positioning System radio occultation (GPS-RO) data from the Constellation Observing System for the Meteorology, Ionosphere, and Climate (COSMIC) mission. The data was obtained from the COSMIC RO Data Analysis and Archive Center (CDAAC:https://cdaac-www.cosmic.ucar.edu/cdaac/index.html), and included 2007-2011 atmprf, echprf, and sonprf products. The "atmprf" data is a product provided by COSMIC. It assumes that the atmosphere is dry air and provides dry temperature values from the ground to 0.2 hPa. "echprf" is obtained by interpolating the data on the ECMWF high-resolution grid onto the occultation profile, including the pressure profile, temperature profile, water vapor pressure profile, refractivity profile, and bending angle profile. "sonprf" is obtained by interpolating NCAR's radiosonde data onto the occultation profile, and has temperature, pressure, humidity and refractivity profile data. The global distribution of GPS-RO profiles is shown in the Figure 1. Note that low numbers of GPS-RO profiles are available in the tropics and high polar regions, whereas high numbers appear in the mid latitudes.

Peer-reviewed version available at Sensors 2020, 20, 4762; doi:10.3390/s20174762

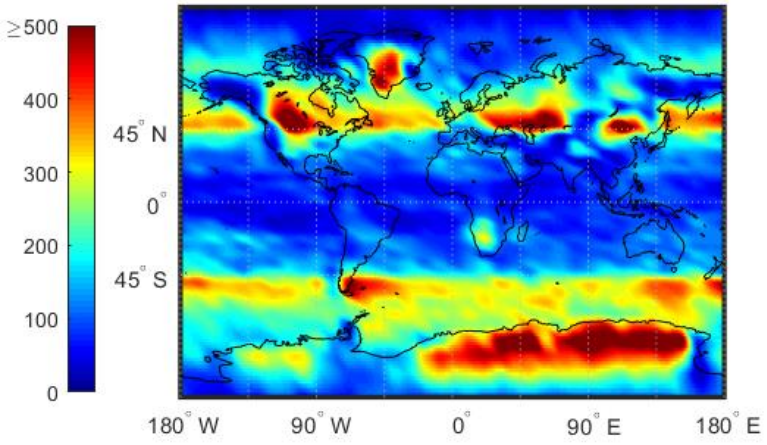

Figure 1. The number of COSMIC GPS-RO profiles from 2007 to 2011 for which the signal penetrates to below 500 m above the surface

3. Methods

Figure 2 shows two occultation atmospheric profiles and two sounding profiles. Each set was selected from the same time and place. Figure 2.a and Figure 2.c depict a significant change in temperature and water vapor; a phenomenon that usually occurs near the PBL top, where the greatest decrease is found in the bending angle, refractivity and temperature vertical profiles. However, there are inevitably high-frequency components in the angle data. If the gradient method of the bending angle is calculated using the difference method, the noise from high-frequency components will interfere with the result. In order to solve this problem, herein, we propose a new numerical differentiation method. The model function method determines the regularization parameters to obtain the angle profile, and then uses the maximum gradient method to obtain the MBLH. The specific method steps are described below.

Peer-reviewed version available at Sensors 2020, 20, 4762; doi:10.3390/s20174762

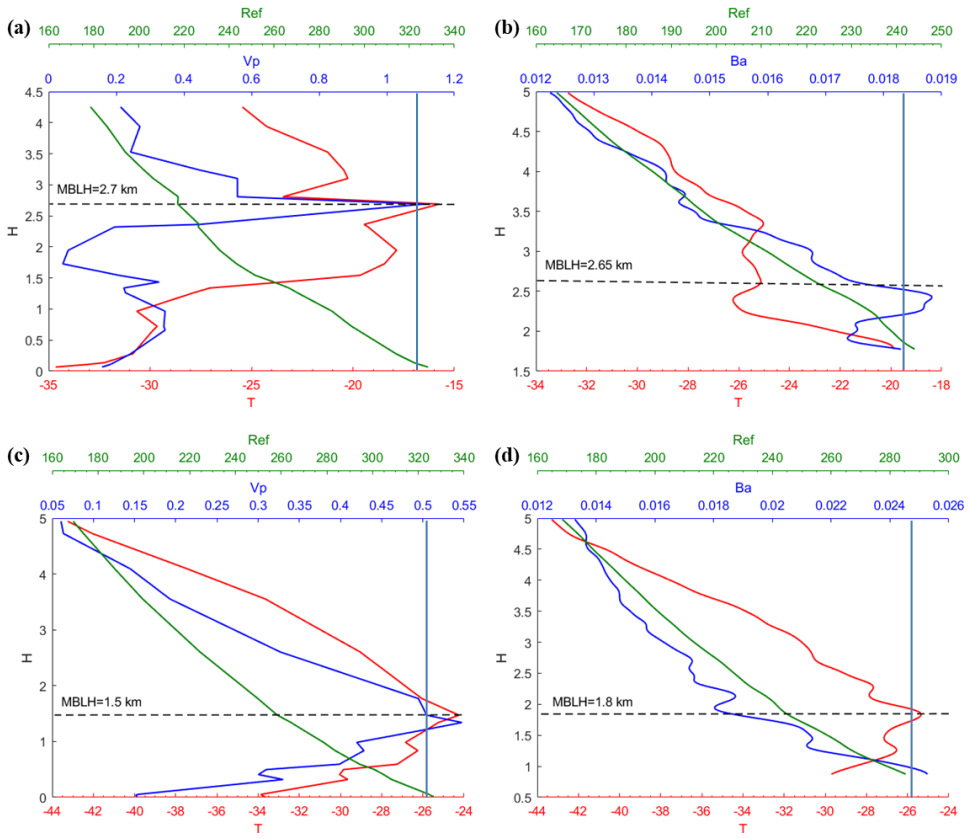

Figure 2. An example of two GPS-RO atmprfs and sonprfs matched at the $(67.3^{o}N, 87.9^{o}W)$ and $(79.2^{o}N, 59.3^{o}W)$ respectively. The elliptical shaded region represents the high frequency part of the occultation bending angle profile.

Suppose that the bending angle profile is a continuously differentiable function— $BA(z)$, z is the height above sea level $z_i = z_1 + (i-1)h, i = 1, \mathrm{L}\ , m$, where $z_b = z_1 < z_2 < \mathrm{L}\ < z_{m-1} < z_m = z_t$ is a one-dimensional uniform grid with a fixed vertical interval h. $BA(z)$ is given by the COSMIC data angle profile, and the approximate value of the first derivative of $BA(z)$ is obtained by the following numerical differentiation method.

According to the Newton-Leibniz formula and Simpson formula:

$$BA(z_{i+1}) - BA(z_{i-1}) = \int_{z_{i-1}}^{z_{i+1}} \varphi(z)dz \approx \frac{h}{3}(\varphi_{i-1} + 4\varphi_i + \varphi_{i+1}),\ i = 2, \mathrm{L}\ , m-1, \tag{3}$$

The matrix expression of equation *(4)* is:

$$\mathbf{AX} = \boldsymbol{b}, \tag{4}$$

Where,

Peer-reviewed version available at Sensors 2020, 20, 4762; doi:10.3390/s20174762

$$\mathbf{A}=\begin{pmatrix} 1 & 4 & 1 & & \\ & \mathrm{O} & \mathrm{O} & \mathrm{O} & \\ & & 1 & 4 & 1 \end{pmatrix},\ \mathbf{X}=(\varphi_1,\varphi_2,\mathrm{L}\ ,\varphi_{m-1},\varphi_m)^{\mathrm{T}},$$

$$\boldsymbol{b}=\left(\frac{3}{h}(BA_3-BA_1),\ \frac{3}{h}(BA_4-BA_2),\ \mathrm{L}\ ,\ \frac{3}{h}(BA_{m-1}-BA_{m-3}),\ \frac{3}{h}(BA_m-BA_{m-2})\right)^{\mathrm{T}},$$

However, if the observation data in equation (4) has high-frequency components, inverting the atmospheric bending angle vertical gradient will produce a result with large errors. Therefore, in order to overcome the ill-posedness of equation (4), we transformed the solution into a problem that requires solving the objective functional minimum value as follows:

$$J(x)=\frac{1}{2}\|Ax-b\|^2+\frac{\alpha}{2}\|Lx\|^2+\frac{\beta}{2}\|x\|^2, \tag{5}$$

$$X=\arg\min_x J(x)=(\alpha L^TL+A^TA+\beta I)^{-1}A^Tb, \tag{6}$$

Where, X is a solution that satisfies the functional minimum, α,β is the biregularization parameter that needs to be determined and the specific method will be discussed below, and the matrix L is the first derivative operator which means constrain to x ; thus the last two regulation terms in the equation (5) will make the gradient oscillation of x more moderate and produce a smooth effect.

$$L=\begin{bmatrix} -1 & 0 & 1 & & \\ & -1 & 0 & 1 & \mathrm{O} \\ & \mathrm{O} & \mathrm{O} & \mathrm{O} & \mathrm{O} \\ & & & -1 & 0 & 1 \end{bmatrix}_{(n-2)\times n}$$

In this paper, a double-parameter model function method [22,23] was used to determine the optimal solution of the two parameters α,β in the objective functional, and then obtain the bending angle gradient. The basic technical route is as follows:

The objective function $F(\alpha,\beta)$ is:

$$F(\alpha,\beta):=\min_{x\in X}J(\alpha,\beta;x)=\frac{1}{2}\|Ax-b\|^2+\frac{\alpha}{2}\|Lx\|^2+\frac{\beta}{2}\|x\|^2, \tag{7}$$

The damped Morozov deviation equation is：

$$G(\alpha,\beta):=F(\alpha,\beta)+(\alpha^{\gamma}-\alpha)\frac{\partial F(\alpha,\beta)}{\partial\alpha}+(\beta^{\mu}-\beta)\frac{\partial F(\alpha,\beta)}{\partial\beta}-\frac{1}{2}\delta^2=0, \tag{8}$$

where, $\gamma>1,\mu>1$ are damped coefficient and δ measures the error. Because equation *(8)* is a nonlinear equation concerning α,β , solving it by the usual iterative method (such as the Newton method and quasi-Newton method) is not ideal; as they only have the property of local convergence, and the requirements for the initial value are relatively high. Therefore, we employed a model function method, that has been widely used in recent years, to determine the regularization parameters. The model function method is advantageous in that the amount of calculating is greatly reduced, and the convergence is guaranteed. While there are various model function options, for simplicity, we opted to use a linear model function $m_k(\alpha,\beta)$ to approximate $F(\alpha,\beta)$ after k iterations, where:

Peer-reviewed version available at Sensors 2020, 20, 4762; doi:10.3390/s20174762

$$m_k(\alpha,\beta) := T_k + \alpha C_k + \beta D_k \to F(\alpha,\beta),$$
$$T_k = \frac{1}{2}\left\|Ax_k - b\right\|^2, C_k = \frac{1}{2}\left\|Lx_k\right\|^2, D_k = \frac{1}{2}\left\|x_k\right\|^2, \quad (9)$$

Substituting equation (9) into equation (8):

$$G(\alpha,\beta) := m_k(\alpha,\beta) + (\alpha^\gamma - \alpha)\frac{\partial m_k(\alpha,\beta)}{\partial \alpha} + (\beta^\mu - \beta)\frac{\partial m_k(\alpha,\beta)}{\partial \beta} - \frac{1}{2}\delta^2 = 0, \quad (10)$$

Next, the regularization double parameters α, β were determined as concisely summarized in Figure 3:

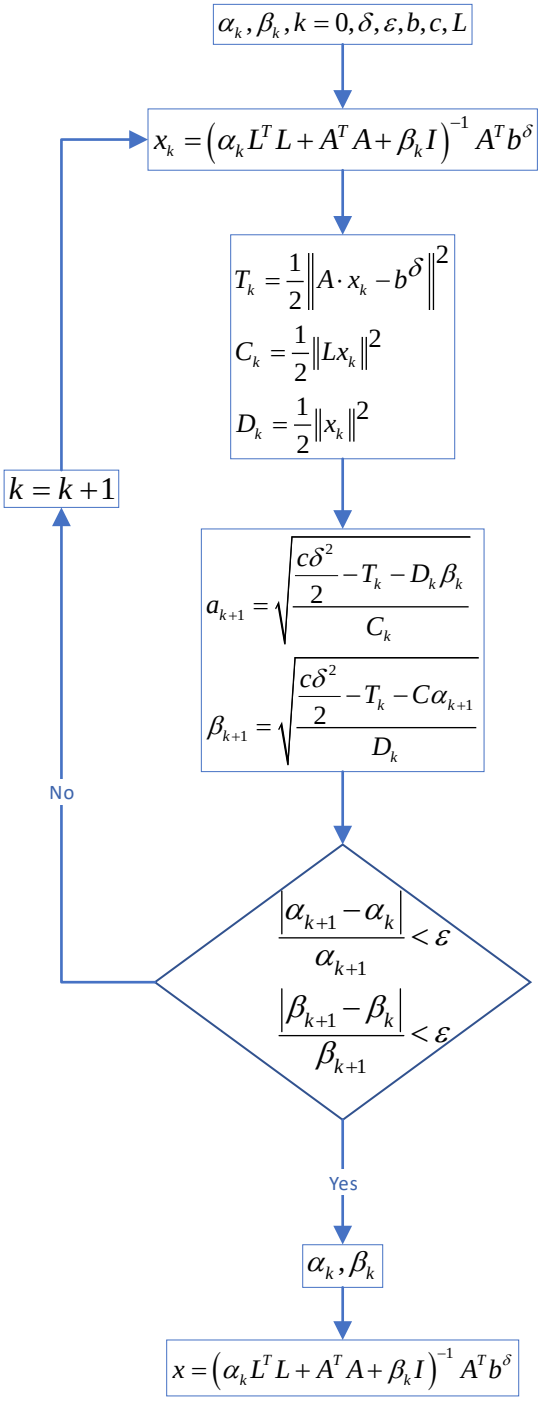

Peer-reviewed version available at Sensors 2020, 20, 4762; doi:10.3390/s20174762

Figure 3. Flow chart for determining double regularization parameters using the model function method

4. Climate characteristics of MBLH

4.1. Subsection

Figure 4 shows the distribution characteristics of the average MBLH in the global ocean. Note that the MBLH over the ocean closely correlates with the cold or warm ocean currents underlying the surface(Figure 5). On the west coast of the mainland, cold ocean currents overlap with low boundary layer height areas. These areas are accompanied by subsidence airflow, and the inversion layer height is relatively low; thus the MBLH obtained from the minimum angle gradient is low. For the same reason, on the east coast of the mainland, the warm ocean currents overlap with the high-value area at the boundary layer. The MBLH in the low latitude region is about 2.5-3 km, and the MBLH in the high latitude region is about 1 km. Essentially, there are more solar radiation hours in the low latitude region, and the rising air mass carries a large amount of condensation latent heat, which can reach the troposphere height. In contrast, the underlying surface in the high latitude region is stable and cold, and the corresponding boundary layer height is low. Thus, the MBLH height gradually decreases from the equator to the poles.

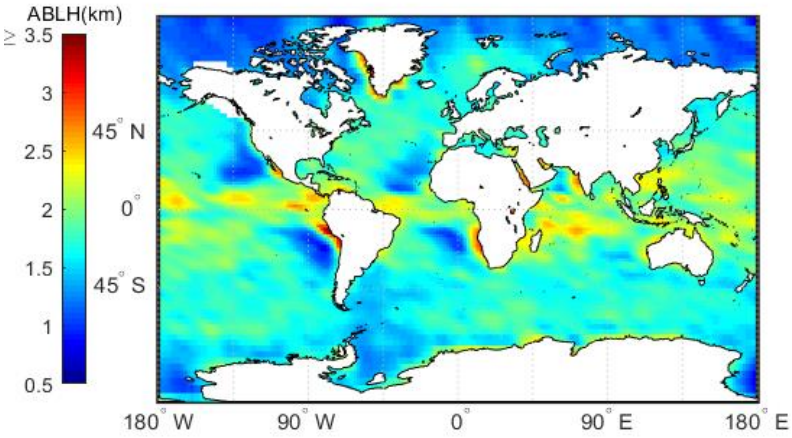

Figure 4. Annual MBLH based on the 2007 - 2011 CDAAC "atmprf" bending angle products.

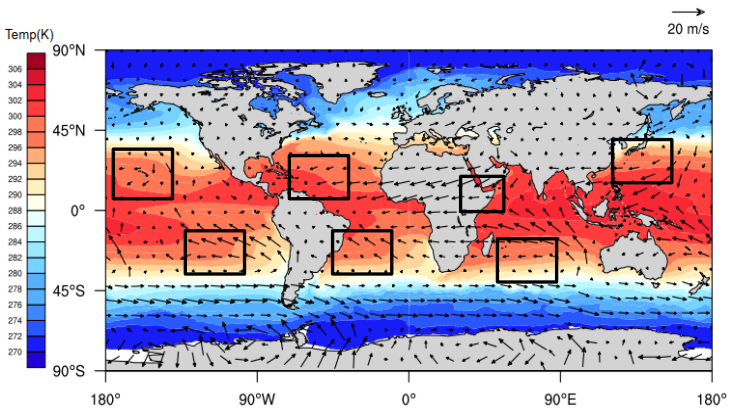

Figure 5. The Annual mean wind-driven current represented by annual mean sea surface temperature field and wind field.The black boxes indicate cold currents.

Peer-reviewed version available at Sensors 2020, 20, 4762; doi:10.3390/s20174762

4.2. Seasonal variation characteristics

The numerical regulation method, in combination with the atmprf and echprf products from CDAAC, were used to comprehensively analyze the seasonal variation characteristics of the global ocean boundary layer's height. Figure 6 shows the monthly average boundary layer height (h_atm) obtained from atmprf data. Note that ocean areas near the Brazilian, California, Canary, and Bengra cold currents have a lower MBLH. This can be explained by the fact that the underlying surface temperature is lower than that of the nearby sea area and the sea surface wind blows from low temperature to high temperature along the direction of temperature gradient, as depicited in Figure 7, from which we can also see the MBLH is proportional to the wind speed from high to low SST and the SST gradient. For the northern and southern equatorial currents, the boundary layer is highest in April. In the westerly current region of the southern hemisphere, the MBLH is stable and maintains at ~2 km. In contrast, in the westerly current region of the northern Hemisphere, the westerly current is blocked to the west due to the existence of the continent, and therefore forms a cold and warm current. The west coast of the continent is lower at ~ 1 km, and the east coast of the continent is higher at ~ 2 km. In January and April, the MBLH is basically situated below 1 km in the Arctic, and 1 - 1.5 km in the waters around Antarctica; while in July and October, the MBLH is located at 1.5 - 2 km in the Arctic, and ~ 1 km in the waters near Antarctica.

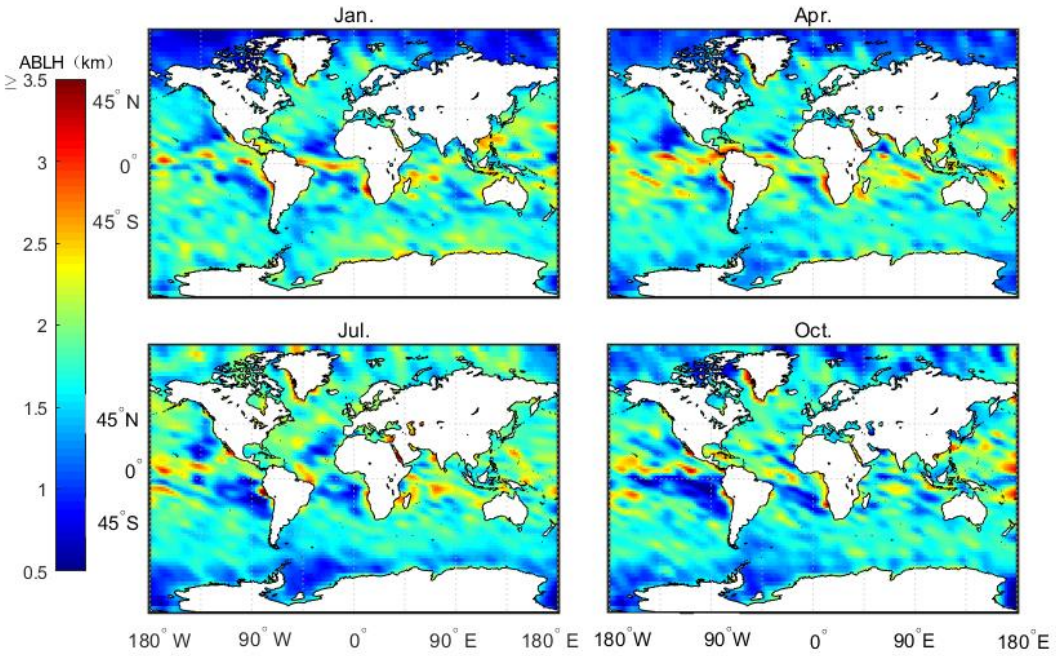

Figure 6. Average MBLH over four months based on the 2007 - 2011 CDAAC "atmprf" bending angle products.

Peer-reviewed version available at Sensors 2020, 20, 4762; doi:10.3390/s20174762

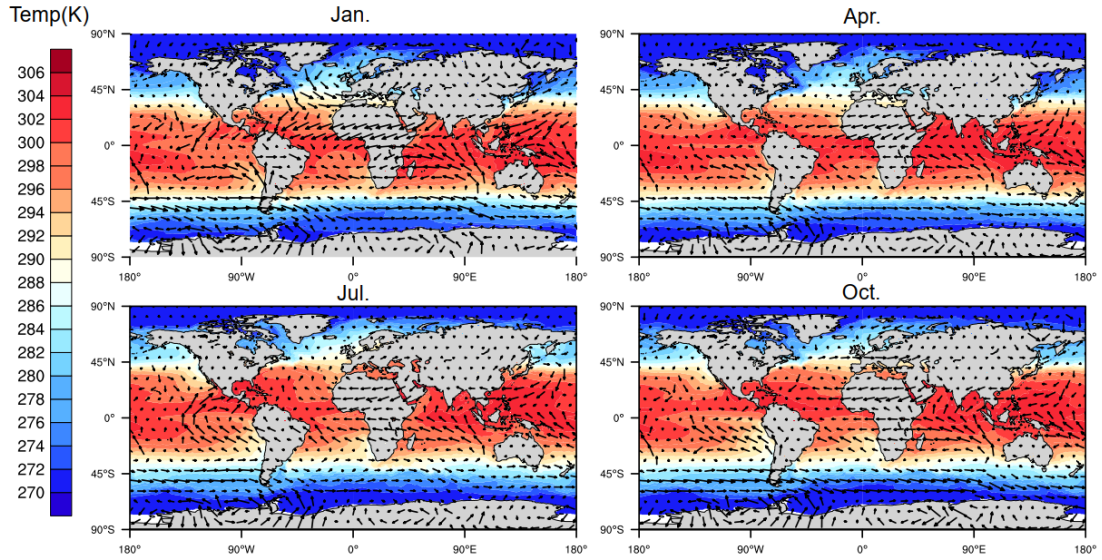

Figure 7. The perennial average monthly wind-driven current represented by monthly mean sea surface temperature field and wind field.

Figure 8 shows the monthly average boundary layer height (h_ech) obtained from echprf data. Note that in January and April, the MBLH reaches a height of 3 km, especially in the westerly ocean current area of the southern hemisphere. Contrarily, in July and October, the MBLH is lower than the heights observed in January and April. With the exception of the westerly ocean currents region, where the MBLH can reach 2.5 km, during the months of July and October, the MBLH remains below 2 km in all the remaining regions. The explanation for this phenomon is as follows: In winter, the ocean surface is warm. As such, the water vapor rises, releasing latent heat at a certain height. This results in the formation of the strongest inversion layer produced throughout the four seasons [17], which pushes the MBLH higher. In contrast, during summer, the ocean surface temperature is lower. Thus, the heating mass in the ocean moves to the cold ocean surface, and easily forms a low-temperature inversion layer, thereby maintaining a relatively low MBLH. The MBLH gradually increases across the mainland from the low stratus area on east coast to the deep convective area on the west coast—especially in the ITCZ area, where the MBLH can reach 2.5 km during January and April. These results parallel those depicted in Figure 6, which shows that the west coast of the continent, where the cold current pass (e.g. Brazil cold current) corresponds to the area with the lower MBLH, and the area's outline corresponds to the cold current flow direction. The direction of the current up the coast correlates with the wind direction. For the westerly jet, the North American mainland coastline and the European coast determines whether it is the California cold current or the North Atlantic warm current.

Peer-reviewed version available at Sensors 2020, 20, 4762; doi:10.3390/s20174762

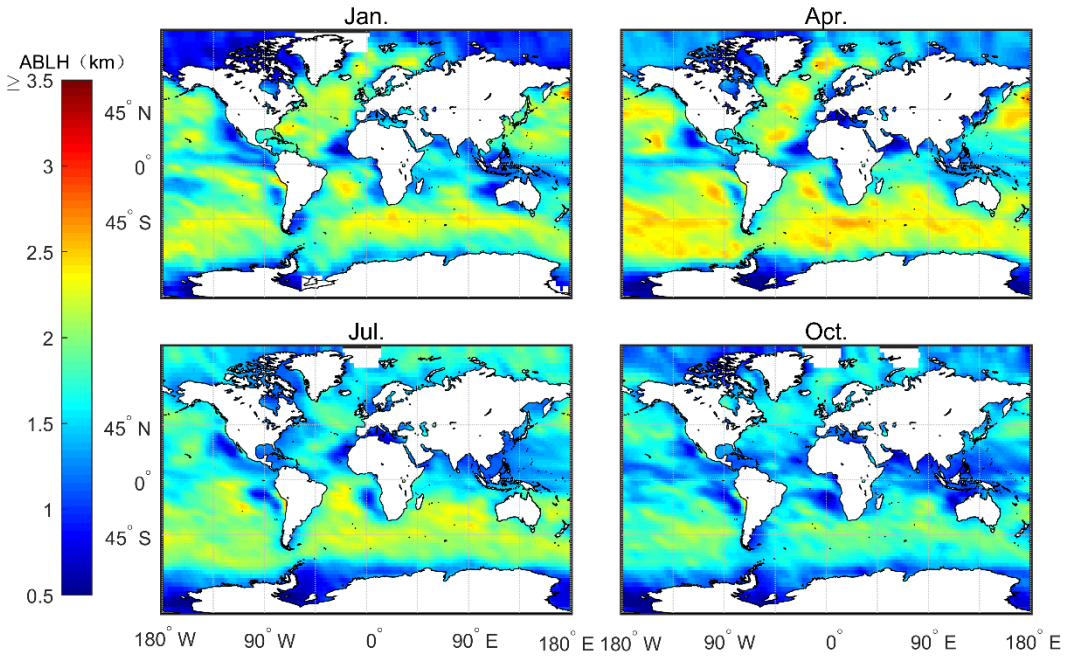

Figure 8. Average MBLH over four months based on the 2007 - 2011 CDAAC "echprf" bending angle products.

Figure 9 shows the gap between h_atm and h_ech. Note that in January and April, h_atm is higher in the low latitude areas, such as the ITCZ area, while h_ech is higher in the southern hemisphere's westerly jet region and the northern hemisphere's middle and high latitudes. In July and October, convection activities in the northern hemisphere are strong. Thus, h_atm is higher than h_ech, and the gap between the two in the southern hemisphere has decreased. In summary, these results imply that h_atm is more sensitive to convective cloud top capture, and is generally higher than h_ech where convection is active.

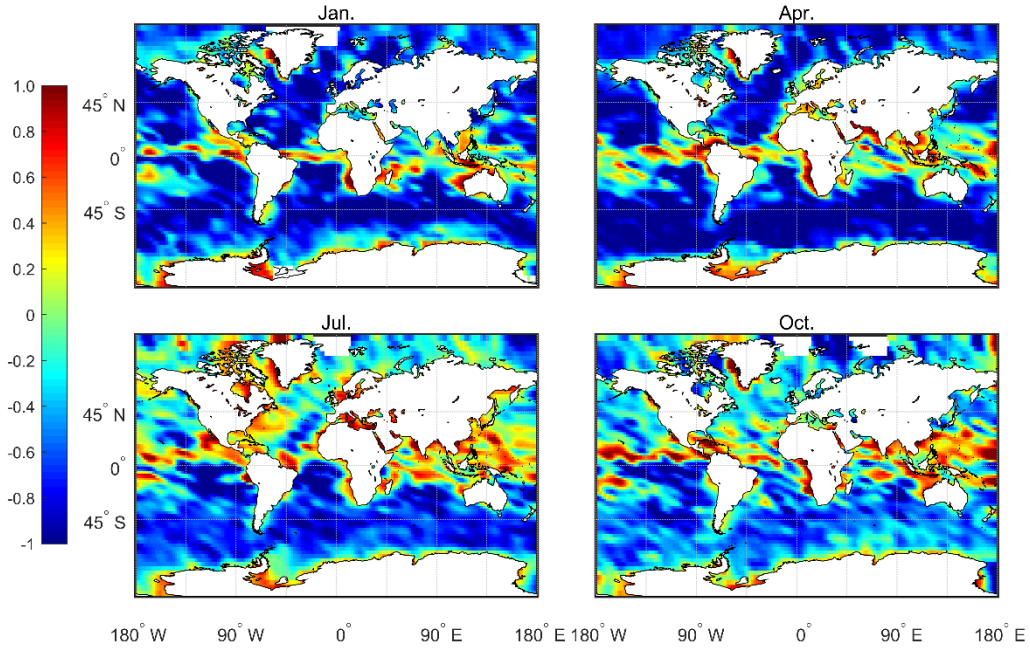

Figure 9. The difference between average MBLH based on 2007 – 2011 CDAAC "echprf" and "atmprf"

Peer-reviewed version available at Sensors 2020, 20, 4762; doi:10.3390/s20174762

products

Figure 10 shows the distribution of atmprf data standard deviation. Note that the standard deviation value is very high (> 0.5) in the low-latitude ocean, especially in the ITCZ area and regions dominated by and downwind from the subtropical trade winds. In contrast, the January and April mid-high latitude standard deviations are low, while the July and October high and low latitude standard deviations are high. A possible explanation is that convection is active in low-latitude areas, thus, there are multiple inversion layers. High-latitude regions are mostly high-level clouds that are uniform and thin. At the same time, comparing Figure 1 and Figure 10 shows that the number of occultation profiles also greatly affects the standard deviation of the results.

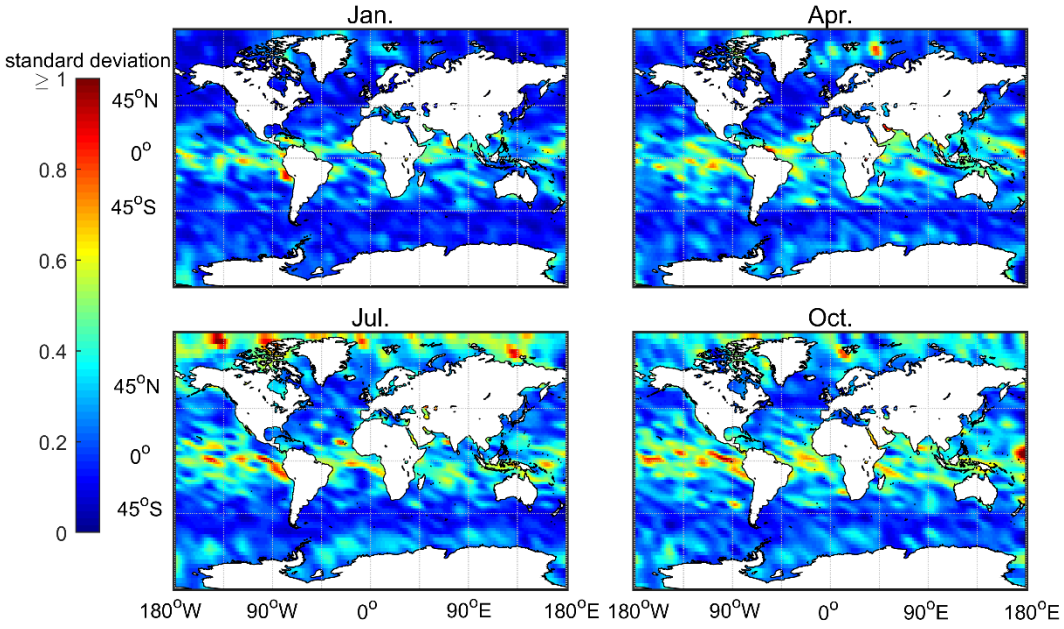

Figure 10. The distribution of standard deviation for the average MBLH over four months, based on COSMIC's 2007 – 2011 'atmprf' bending angle data.

4.3. Interannual variation trend of MBLH and A case study in the South China Sea

Two primary modes of global MBLH were analyzed, as were the time coefficients. As shown in Figure 11(a), the variance contribution rate of the first mode reached 96%. The MBLH decreased from low latitude to high latitude, from the west coast of the mainland to the westward, and corresponded to cold and warm ocean currents, respectively. The time series of the first mode is seasonally distributed. As shown in Figure 11(b), the variance contribution rate of the second mode reached 2.2%. Note that the MBLH anomaly spatial distribution is opposite in the northern and southern hemispheres. The time coefficient demonstrates that it is related to the north-south movement of the direct sun point.

Peer-reviewed version available at Sensors 2020, 20, 4762; doi:10.3390/s20174762

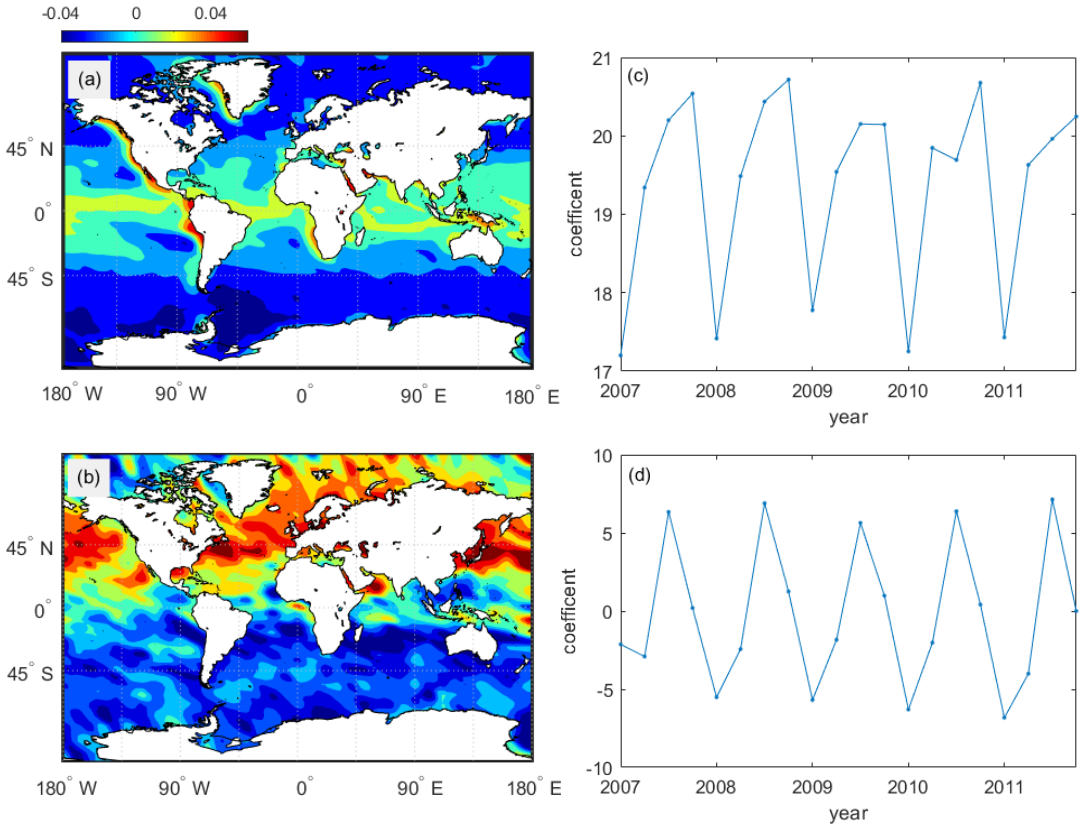

Figure 11. a,b: The two modes of MBLH global distribution from 2007 to 2011. The colorimetric region is the MBLH anomaly; c,d: The time coefficient corresponding to two modes.

Figure 12 shows the MBLH interannual variability from 2007-2011 in parts of the South China Sea (latitude range: $15^{o}N-25^{o}N$, longitude range: $105^{o}E-115^{o}E$). The numbers were derived from 2007 - 2011 COSMIC atmprf, echprf, and sonprf data. The bending angle served as the variable in the first two2 sources, and refractivity in the latter. The results show that the MBLH has undergone a downward trend over the past 5 years, and parallel those reported by Guo, Li, Cohen, Li, Chen, Xu, Liu, Yin, Hu and Zhai [5] for the BLH trend over mainland China. The MBLH obtained by the atmprf data is the largest, the result obtained by the sonprf data is the smallest; and the atmprf results approximate those obtained using echprf. This figure also shows that the MBLH over the South China Sea is highest in January and lowest in July. In January, the South China Sea was in the ascending branch of the land-sea circulation, and convection was active, which was conducive to development of the boundary layer height. In July, it was in the sinking branch, and the lower temperature inversion layer was not conducive to boundary layer development.

Peer-reviewed version available at Sensors 2020, 20, 4762; doi:10.3390/s20174762

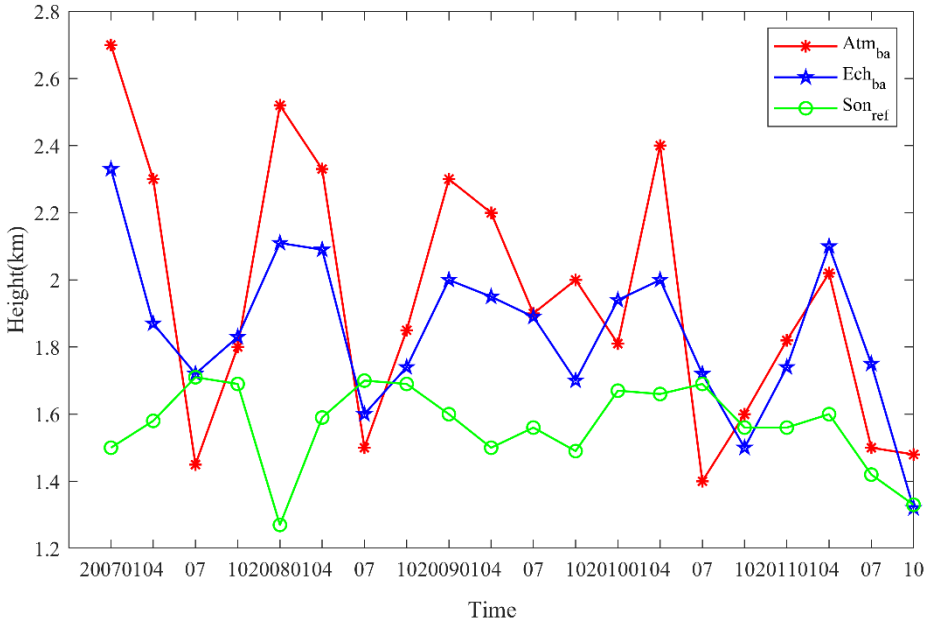

Figure 12. The interannual variability of MBLH in the waters near the South China Sea was derived from COSMIC's atmprf and echprf bending angle and sonprf refractivity

5. Conclusions

Herein, we estimate the global MBLH using GPS-RO profiles from the FORMOSAT-3/COSMIC satellites. We propose a new numerical differential regularization method to analyze and compare the MBLH based on three CDAAC products—atmprf,echprf, and sonprf. MBLH climate characteristics were investigated, and the results can be summarized into the following points:

(1) The average MBLH global distribution demonstrates that over the ocean, the height of the boundary layer is closely correlated with the cold and warm ocean currents underlying the surface. The MBLH is relatively low in the sea area near cold ocean currents, and relatively high in the sea area near warm ocean currents.

(2) MBLH seasonal changes obtained by atmprf, show that in the westerly ocean current area of the southern hemisphere, MBLH is stable and maintained at ~ 2 km; the western coast of the northern hemisphere mainland is ~ 1 km lower; and the eastern coast of the mainland is ~ 2 km higher. For the South China Sea region, the MBLH is situated at ~2.5 km in January, yet the boundary layer is located at 1.5 - 2 km in July. For the bipolar regions, in January and April, the MBLH is low in the Arctic Ocean, and high in the offshore waters of Antarctica; and the results are reversed in July and October.

(3) MBLH seasonal changes obtained by echprf show that in January and April, the MBLH is very high, and can reach 3 km, especially in the westerly current area of the southern hemisphere. Contrarily, in July and October, the MBLH is lower than the heights observed in January and April. Except for the westerly ocean currents region, where the MBLH can reach 2.5 km, during the months of July and October, the MBLH remains below 2 km in all the remaining regions. In essence, during winter, the ocean surface is warm. As such, the water vapor rises, releasing latent heat at a certain height. This results in the formation of the strongest inversion layer produced throughout the four seasons, which pushes the MBLH higher. During summer, the ocean surface temperature is lower. Thus, the heating mass in the ocean moves to the cold ocean surface, and easily forms a low-temperature inversion layer, thereby maintaining a relatively low MBLH. The MBLH gradually increases across the mainland from the low stratus area on east coast to the deep convective area on the west coast—especially in the ITCZ area, where the MBLH can reach 2.5 km during January and April.

Peer-reviewed version available at Sensors 2020, 20, 4762; doi:10.3390/s20174762

(4) A comparison of the results obtained from atmprf and echprf demonstrate that atmprf is more sensitive to convective cloud top capture. Where convection is active, the calculated height of the armprf bending angle is higher than that of echprf, and vice versa.

(5) The MBLH obtained from atmprf has a higher standard deviation in low latitudes and a lower standard deviation in mid-high latitudes. This may be due to active convection in low latitudes, multiple inversion layers, and the occultation profile. The distribution of occulation profile numbers also has a greater relationship.

(6) Through EOF decomposition of the global MBLH, we determined that the first mode is very consistent with the ocean current and that the time coefficients are positive. In contrast, the second mode is related to the periodic change of the sun's direct point, and the northern and southern hemispheres have opposite anomalies. The time coefficient is positive in January and April and negative in July and October, with obvious seasonal changes.

(7) The interannual changes in parts of the South China Sea indicate that the MBLH exhibited a downward trend from 2007 to 2011.

Based on the results herein, we expect that calculating the average MBLH by the method proposed in this paper and incorporating the results into climate models will significantly improve the accuracy of future climate forecasting.

Author Contributions: Conceptualization, JIANYIN ZHOU and JIE XIANG; methodology, SIXUN HUANG; software, JIANYIN ZHOU; validation, JIANYIN ZHOU, JIE XIANG and SIXUN HUANG; formal analysis, JIANYIN ZHOU; investigation, JIANYIN ZHOU; resources, JIANYIN ZHOU; data curation, JIANYIN ZHOU; writing—original draft preparation, JIANYIN ZHOU; writing—review and editing, JIANYIN ZHOU; visualization, JIANYIN ZHOU; supervision, JIE XIANG; project administration, JIE XIANG; funding acquisition, JIE XIANG.

Funding: This research was funded the National Natural Science Foundation of China (Grant No. 91730304,41575026,41475021)

Conflicts of Interest: The authors declare no conflict of interest.

References

1. Sullivan, P.P.; McWilliams, J.C.; Moeng, C.-H. A grid nesting method for large-eddy simulation of planetary boundary-layer flows. *Bound.-Layer Meteorol* **1996**, *80*, 167-202.

2. Thurston, W.; Fawcett, R.J.; Tory, K.J.; Kepert, J.D. Simulating boundary-layer rolls with a numerical weather prediction model. *Q. J. R. Meteorol. Soc.* **2016**, *142*, 211-223.

3. Stull, R.B. *An introduction to boundary layer meteorology*; Springer Science & Business Media: 2012; Vol. 13.

4. Basha, G.; Kishore, P.; Ratnam, M.V.; Ravindra Babu, S.; Velicogna, I.; Jiang, J.H.; Ao, C.O. Global climatology of planetary boundary layer top obtained from multi-satellite GPS RO observations. *Clim. Dyn.* **2019**, *52*, 2385-2398.

5. Guo, J.; Li, Y.; Cohen, J.B.; Li, J.; Chen, D.; Xu, H.; Liu, L.; Yin, J.; Hu, K.; Zhai, P. Shift in the Temporal Trend of Boundary Layer Height in China Using Long-Term (1979–2016) Radiosonde Data. *Geophys. Res. Lett.* **2019**, *46*, 6080-6089.

6. Zhang, Y.; Seidel, D.J.; Zhang, S. Trends in Planetary Boundary Layer Height over Europe. *J. Clim.* **2013**, *26*, 10071-10076.

7. Dang, R.; Yang, Y.; Li, H.; Hu, X.-M.; Wang, Z.; Huang, Z.; Zhou, T.; Zhang, T. Atmosphere Boundary Layer Height (ABLH) determination under multiple-layer conditions using micro-pulse lidar. *Remote Sens.* **2019**, *11*, 263.

8. Baars, H.; Ansmann, A.; Engelmann, R.; Althausen, D. Continuous monitoring of the boundary-layer top with lidar. *Atmos. Chem. Phys* **2008**, *8*, 7281-7296.

Peer-reviewed version available at Sensors 2020, 20, 4762; doi:10.3390/s20174762

9. Beyrich, F. Mixing height estimation from sodar data — A critical discussion. *Atmos. Environ.* **1997**, *31*, 3941-3953.

10. Bianco, L.; Wilczak, J.M. Convective Boundary Layer Depth: Improved Measurement by Doppler Radar Wind Profiler Using Fuzzy Logic Methods. *J Atmos Ocean Technol* **2002**, *19*, 1745-1758.

11. Liu, B.; Guo, J.; Gong, W.; Shi, Y.; Jin, S. Boundary Layer Height as Estimated from Radar Wind Profilers in Four Cities in China: Relative Contributions from Aerosols and Surface Features. *Remote Sens.* **2020**, *12*, 1657.

12. Siuta, D.; West, G.; Stull, R. WRF hub-height wind forecast sensitivity to PBL scheme, grid length, and initial condition choice in complex terrain. *Weather Forecast.* **2017**, *32*, 493-509.

13. Terra, R.; Mechoso, C.R.; Arakawa, A. Impact of orographically induced spatial variability in PBL stratiform clouds on climate simulations. *J. Clim.* **2004**, *17*, 276-293.

14. Basha, G.; Ratnam, M.V. Identification of atmospheric boundary layer height over a tropical station using high-resolution radiosonde refractivity profiles: Comparison with GPS radio occultation measurements.J. Geophys. Res. Atmos. **2009**, *114*.

15. Ao, C.O.; Waliser, D.E.; Chan, S.K.; Li, J.L.; Tian, B.; Xie, F.; Mannucci, A.J. Planetary boundary layer heights from GPS radio occultation refractivity and humidity profiles.J. Geophys. Res. Atmos. **2012**, *117*.

16. Yehui, Z.; Dian, J.S.; Shaodong, Z. Trends in Planetary Boundary Layer Height over Europe. *J. Clim.* **2013**, *26*, 10071-10076.

17. Chan, K.M.; Wood, R. The seasonal cycle of planetary boundary layer depth determined using COSMIC radio occultation data. J. Geophys. Res. Atmos. **2013**, *118*, 12,422-412,434.

18. Sokolovskiy, S.V.; Rocken, C.; Lenschow, D.H.; Kuo, Y.-H.; Anthes, R.A.; Schreiner, W.S.; Hunt, D.C. Observing the moist troposphere with radio occultation signals from COSMIC. *Geophys. Res. Lett.* **2007**, *34*.

19. Shu-peng, H.; Liang, P.; Richard, A.A.; Ying-Hwa, K.; Hsiao-Chun, L. Marine Boundary Layer Heights and Their Longitudinal, Diurnal, and Interseasonal Variability in the Southeastern Pacific Using COSMIC, CALIOP, and Radiosonde Data. *J. Clim.* **2015**, *28*, 2856-2872.

20. Chien, F.-C.; Hong, J.-S.; Kuo, Y.-H. The marine boundary layer height over the western north pacific based on GPS radio occultation, island soundings, and numerical models. *Sensors* **2019**, *19*, 155.

21. J.R.Garratt. Review: the atmospheric boundary layer. *Earth-Sci. Rev.* **1994**, *37*, 89 - 134.

22. Kunisch, K.; Zou, J. Iterative choices of regularization parameters in linear Inverse Probl.. *Inverse Probl.* **1998**, *14*, 1247.

23. Lu, S.; Pereverzev, S.V. Multi-parameter regularization and its numerical realization. *Numer Math (Heidelb).* **2011**, *118*, 1-31.